



# Influence of a remelt scan strategy on the microstructure and fatigue behaviour of additively manufactured biomedical Ti65Ta efficiently assessed using small scale specimens

Erin G. Brodie <sup>a,b,1,\*</sup>, Julia Richter <sup>c,\*<sup>1</sup></sup>, Thomas Wegener <sup>c,\*<sup>1</sup></sup>, Andrey Molotnikov <sup>a,b,d</sup>, Thomas Niendorf <sup>c</sup>

<sup>a</sup> Department of Materials Science and Engineering, Monash University, Clayton, VIC, 3800, Australia

<sup>b</sup> Monash Centre for Additive Manufacturing (MCAM), 11 Normanby Road, Nottinghill, VIC, 3168, Australia

<sup>c</sup> University of Kassel, Institute of Materials Engineering – Metallic Materials, Moenchebergstrasse 3, 34125, Kassel, Germany

<sup>d</sup> RMIT Centre for Additive Manufacturing, School of Engineering, RMIT University, Melbourne, Australia



## ARTICLE INFO

### Keywords:

Tantalum  
Titanium  
Laser powder bed fusion  
Fatigue  
Biomedical

## ABSTRACT

Due to its high cost and demanding characteristics, Tantalum requires unique processing techniques and is restricted to small parts. In the present work, Ti65Ta was additively manufactured as a new potential material for small biomedical implants. Assessment of the effects of a remelt scanning strategy was solely accomplished by testing of small mechanical specimens. Yield strength was achieved superior to either L-PBF pure Ti or Ta and low-cycle fatigue behaviour was similar to that of L-PBF Ti-6Al-4 V. The Ti65Ta alloy is a good candidate for a new gold standard alloy for small bone interfacing implants.

## 1. Introduction

Additive manufacturing (AM) technologies, especially powder bed fusion processes, have gained importance in the aerospace and medical sectors within the last decade, especially in cases where challenging materials have to be processed, leading to high conventional part production costs [1–3]. Here, the high freedom of design, direct model-to-part production and high dimensional tolerances enabled by the laser based powder bed fusion technique (L-PBF) provide significant manufacturing benefits for bespoke parts. Nickel based superalloy Inconel718, stainless steel 316L and titanium alloy Ti-6Al-4 V were originally the focus of AM investigations [4–6], however recent developments have expanded the AM material toolkit to Al-alloys, tool steels, Mg-alloys and functional materials in order to open up markets in numerous industries [7].

For biomedical implants, Ti-6Al-4 V is used almost exclusively due to its inert, corrosion resistant character and its high strength to weight ratio. Nonetheless, Ti-6Al-4 V was originally developed for aircraft and not for biomedical use. In applications where Ti-6Al-4 V is used for implants which replace large segments of bone, due to its high elastic modulus, stress-shielding can occur around the implant, leading to bone

resorption and implant failure [8,9]. Furthermore, additively manufactured Ti-6Al-4 V solidifies in a brittle martensitic  $\alpha'$  microstructure in the as-built state, requiring post-heat treatments to reintroduce acceptable levels of ductility [10]. The development of new AM biomedical alloys is required to improve both implant mechanical performance and implant-bone integration. One promising alloy system is the titanium-tantalum (Ti-Ta) system. This alloy falls within the class of  $\beta$ -titanium alloys, as at contents of over 45 wt% Ta, a  $\beta$ -phase structure is fully retained, lowering the elastic modulus to half that of pure Ti [11]. In addition, Ta has a long history of use in medicine, building a strong case for its biocompatibility and has recently been highlighted for its ability to enhance bone growth [12–14].

The barriers to using Ta containing alloys in biomedical applications include the difficulties of manufacture and the inherent high density of Ta. Ta, as a refractory metal, melts at approximately 3000 °C, making it difficult and expensive to alloy and manufacture into complex shapes [15]. Furthermore, the high density of Ta restricts its use for large implants as the implant weight is too great, causing stress on surrounding tissues and ligaments. But for small implants, such as mandible reconstruction plates, Ta alloys could provide the benefits of low elastic modulus and enhanced bone integration. L-PBF processes have shown to

\* Corresponding authors.

E-mail addresses: [erin.brodie1@monash.edu](mailto:erin.brodie1@monash.edu) (E.G. Brodie), [julia.richter@uni-kassel.de](mailto:julia.richter@uni-kassel.de) (J. Richter), [t.wegener@uni-kassel.de](mailto:t.wegener@uni-kassel.de) (T. Wegener).

<sup>1</sup> These three authors contributed equally to this work.

be successful at processing this conventionally difficult-to-manufacture metal and also provide the design freedom to manufacture implants which exactly match individual bone structure, particularly subtle facial contours [16,17]. An improved match of implant-bone structure helps to improve both the implant stability, by increasing surface interaction between the implant and bone, and the quality of life of the patient, due to better functionality and aesthetic outcomes [16].

However, the qualification of AM parts across multiple industries has raised concerns in correlating the mechanical response of conventional standardised specimen sizes produced by AM to the performance of complex geometry AM parts [18]. As opposed to conventional manufacture, where both parts and test specimens could be machined from the same bulk material, each AM part has an unique thermal history depending on its geometry [19]. Hence, building conventional dimension mechanical test specimens creates a microstructure with different features to that of the AM part and does not adequately represent the mechanical performance. Thus, to understand the behaviour of a potential new biomedical alloy, Ti65Ta, for small implant devices such as mandible plates, sub-sized mechanical specimens must be investigated.

In the present study, the static and cyclic mechanical properties of L-PBF Ti65Ta were investigated using small specimen sizes for mechanical testing. A mixed powder Ti65Ta alloy was chosen, due to its low modulus potential and high Ta content, and L-PBF parameter optimisation was conducted. Scan speed and scan strategy, specifically the use of a remelt scan, were adjusted and the porosity and volumes of remaining partially melted Ta particles assessed. As the presence of defects and partially melted particles have the potential to strongly affect mechanical properties in small specimen sizes, as they contribute to a significant percentage of the cross-sectional area, these features were explored by both optical microscopy and micro-computed tomography ( $\mu$ -CT). The optimal processing parameters were then used to manufacture small tensile and fatigue specimens, and these were tested in both the single melt and remelt scanning conditions. Electron back scattered diffraction (EBSD) images of the microstructure were coupled with the mechanical data to determine the suitability of the L-PBF Ti65Ta alloy for small implant applications.

## 2. Materials and methods

### 2.1. Laser powder bed fusion (L-PBF) of Ti65Ta

Spherical plasma atomised tantalum (TEKNA, Canada) and commercially pure titanium gas-atomised (Grade 1 ASTM B861, TLS Technik Spezialpulver, Germany) powders were tumble mixed for 12 h at 15 rpm. The particle diameters ranged from 15 to 45  $\mu\text{m}$ . Parameter optimisation and manufacturing of mechanical testing specimens were conducted using a Concept Laser Mlab Cusing R, under an argon atmosphere. For parameter optimisation, scanning speeds from 200 – 400  $\text{mm/s}$  were assessed at a constant laser power of 95 W, close to the maximum power achievable by the machine. The laser hatching was a continuous line scan running 45° to the x-axis and a 90° rotation of the scan path was applied between layers. Due to the refractory nature of the Ta constituent, a remelting scan strategy was also tested to improve material homogeneity. The remelt scan consisted of a second laser pass per layer, with identical scanning parameters. The laser scan path was also identical to the first laser pass.

Cubes with an edge length of 10 mm were used for process parameter development and were assessed optically for both porosity and remaining partially melted Ta particle area. Once optimised parameters had been determined, specimen cuboids (c.f. Fig. 1 (b)) were manufactured for tensile and fatigue testing. Specimens were electro-discharge machined (EDM) from the centre of the cuboid to the dimensions shown in Fig. 1. Small specimens as shown in Fig. 1 (a) were designed (in accordance with ASTM standard E8) to only require a maximum of 40 mm of powder in the MLab Cusing R powder delivery system.

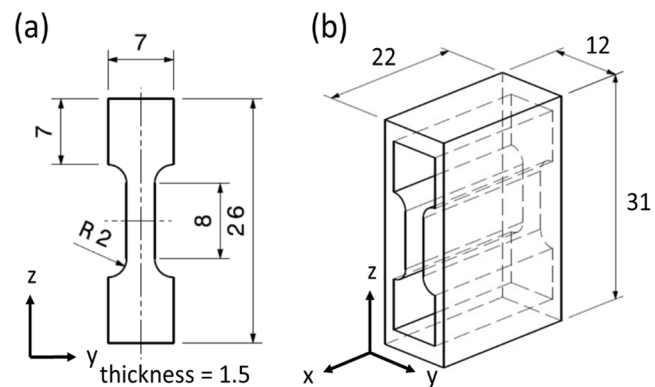


**Fig. 1.** Dimensions of the small specimens used for mechanical testing (a) electro-discharge machined from the L-PBF processed block (b). All measurements are in mm.

### 2.2. Microstructure characterisation

$\mu$ -CT measurements were conducted to evaluate the porosity and remaining Ta particle distribution to a higher accuracy than optical analysis. Due to low penetration depths of X-rays in Ta, specimens with a size of  $0.5 \times 0.5 \times 2 \text{ mm}^3$  were cut with a diamond wire saw. The specimens were probed using a Zeiss Xradia Versa 520 operating at an acceleration voltage of 140 kV and a power of 10 W. The achieved voxel size was  $2.2 \mu\text{m}$ . The reconstruction of the raw data was performed with Avizo 9.4 software. Based on the grey values, pores as well as residual Ta particles were separated from the bulk material. Minor measuring artefacts ( $<5\mu\text{m}$  in equivalent diameter) were excluded during post processing. For all pores and Ta particles an equivalent diameter was calculated, representative of a similar volume to the analysed feature.

The microstructure of the L-PBF material was assessed in both the x-y and y-z planes using electron back-scattered diffraction (EBSD). Specimens were mechanically ground and polished with  $0.04 \mu\text{m}$  OPS solution and imaged using a JEOL 7001 FEG SEM at 20 kV accelerating voltage. Grain size was determined using the line intercept method over 8000 grains for the single melt specimen and 15,000 grains for the remelt specimen.

### 2.3. Mechanical testing

Tensile specimens with gauge dimensions of  $8 \times 3 \times 1.6 \text{ mm}^3$  were cut by EDM as displayed in Fig. 1 and afterwards ground to P1200. Tensile tests were conducted under displacement control with a constant crosshead speed of 2 mm/min until fracture, using a screw-driven MTS criterion load frame with a maximum load capacity of 20 kN. The strain was measured by a contact extensometer with a gauge length of 5 mm.

For low-cycle fatigue (LCF) testing, the same dog bone shaped specimens were cut and ground as for tensile testing. The tests were conducted on a servo-hydraulic testing machine under total strain control in fully reversed push-pull loading ( $R_e = -1$ ) at a constant strain rate of  $6 \times 10^{-3} \text{ s}^{-1}$ . Strain amplitudes of  $\Delta\varepsilon_t/2 = \pm 0.5\%$ ,  $\Delta\varepsilon_t/2 = \pm 0.65\%$  and  $\Delta\varepsilon_t/2 = \pm 0.8\%$  were considered and strain was measured by a 5 mm contact extensometer. After LCF testing, the fracture surfaces were examined using a high resolution scanning electron microscope Zeiss ULTRA GEMINI operating at an acceleration voltage of 20 kV.

## 3. Results

### 3.1. Parameter optimisation and microstructural evolution

The range of scan speeds tested was a modified processing window based on the parameter optimisation study of a Ti25Ta alloy [20]. Hence the resulting relative density range was narrow, with all specimens

showing densities > 99.8 % (Fig. 2 (a)). For both the single scan and remelt scan specimens, porosity increased at speeds below 300 mm/s and above 400 mm/s. These speeds represent the energy density processing limits for the mixed Ti-Ta powders. At speeds below 300 mm/s, porosity increases as high energy causes vaporisation in the Ti constituent (c.f. Fig. 2 (b)), whilst at 400 mm/s, not enough energy is provided to induce complete melting between the Ti and Ta particles. The remelt scan showed a negligible effect on densification across the speeds investigated. The optical micrograph in Fig. 2 (c) reveals a high density at a scan speed of 350 mm/s.

The remaining area of partially melted Ta particles decreased with decreasing scan speed, as the energy density during the build increased (c.f. Fig. 2 (d)). The remelt scan was effective at decreasing the remaining area of Ta particles by approximately 0.4 % on average, compared with the same scan speeds using the single melt strategy. Hence, the optimal scanning speed of 350 mm/s was chosen and specimens for mechanical testing were produced with both the single melt and remelt scanning strategies to further investigate the effect of partially melted particles on mechanical behaviour. The corresponding electron back scattered images, revealing the influence of remelting on the distribution of Ta particles, are displayed in Fig. 2 (e) and (f).

Due to the nature of the small specimens to be used for mechanical testing, and the size of the remaining defects and partially melted Ta particles highlighted by optical analysis, it was deemed necessary to further characterise the porosity and partially melted particle morphology and distribution present in the specimens using  $\mu$ -CT analysis (Fig. 3).

The  $\mu$ -CT analysis confirmed the presence of pores as well as partially melted Ta particles for both scan strategies. The single melt material possessed a high relative density of 99.88 % and remelting slightly increased the density to 99.97 %. The equivalent pore diameter for both conditions was between 10 and 30  $\mu$ m (c.f. Fig. 3 (a)). In the single melt condition, the sphericity of the pores decreased with an increasing size of the equivalent diameter, as shown in Fig. 3 (b). After remelting this correlation became less distinct, as a higher number of smaller pores are created, characterised by a low sphericity. The  $\mu$ -CT scan of the single

melt specimen revealed a high amount of residual partially melted Ta, which was considerably decreased by remelting (from 3.25 % to 0.96 %). The single melt specimen featured Ta particles with sizes between 10 and 50  $\mu$ m (with a peak at 15  $\mu$ m). As is shown in Fig. 3 (c), remelting led to a shift of the maximum Ta particle size to 20  $\mu$ m, however, the same range of sizes was retained. The Ta particles in the single melt specimen were highly spherical, however the perfect sphericity (particles with sphericity of 1) was reduced by consecutive remelting (c.f. Fig. 3 (d)).

Finally, EBSD analysis was undertaken to observe the underlying grain morphology present in the small size specimens (c.f. Fig. 4). The microstructure observed was fully  $\beta$ -phase, as expected for TiTa compositions above 45 wt% Ta [11]. The x-y plane of the specimens revealed a microstructure in which the scan pattern could be identified. Laser scan tracks of approximately 35  $\mu$ m in width were observed at 45° across the specimen plane. The grain size in the single scan specimen (Fig. 4 (a)) is non-homogeneous across the area investigated, whilst the remelt scan specimen (Fig. 4 (b)) showed a refined grain size with reduced variability. The refined grain size induced by the remelt scan was also observed in the y-z plane (Fig. 4 (c), (d)). Considering both the x-y and y-z planes, the single scan and remelt scan specimens showed average grain sizes of  $4.8 \pm 5.6 \mu\text{m}$  and  $3.3 \pm 2.9 \mu\text{m}$ , respectively.

Most importantly, the y-z plane is characterised by an absence of columnar grains and instead, curved grains, which appear to mimic the shape of the base of the melt pool, are seen (Fig. 4 (c)). When the remelt scan was applied, these curved grains were replaced with smaller elongated grains, radiating in a curve outlining the melt pool boundary (circled regions in Fig. 4 (d)).

### 3.2. Tensile behaviour

The tensile stress-strain response of the small specimens was investigated to deduce the (quasi)static mechanical properties of the L-PBF Ti65Ta material (Fig. 5 (a)). Representative stress-strain curves are shown for the single melt and remelt conditions. The single melt specimens were characterised by a yield strength (YS) and ultimate tensile strength (UTS) of 740 MPa and 820 MPa, respectively. The specimen

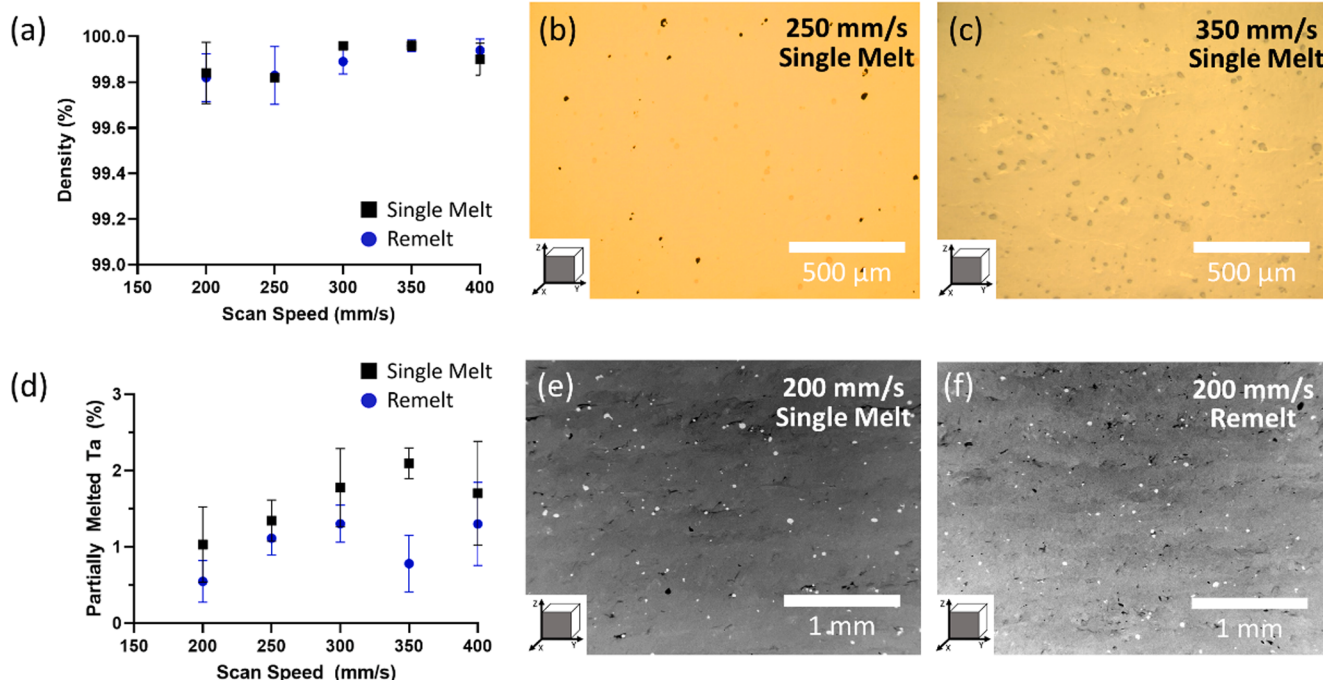


**Fig. 2.** L-PBF processing window of the Ti65Ta alloy showing the effects of scan speed on the relative density –a - c) and a remelt scan on the occurrence of partially melted Ta –d - f). Optical micrographs are shown in (b) and (c) with processing defects (black) and partially melted Ta particles (grey). Electron backscatter images in (e) and (f) show both defects (black particles) and partially melted Ta particles (white).

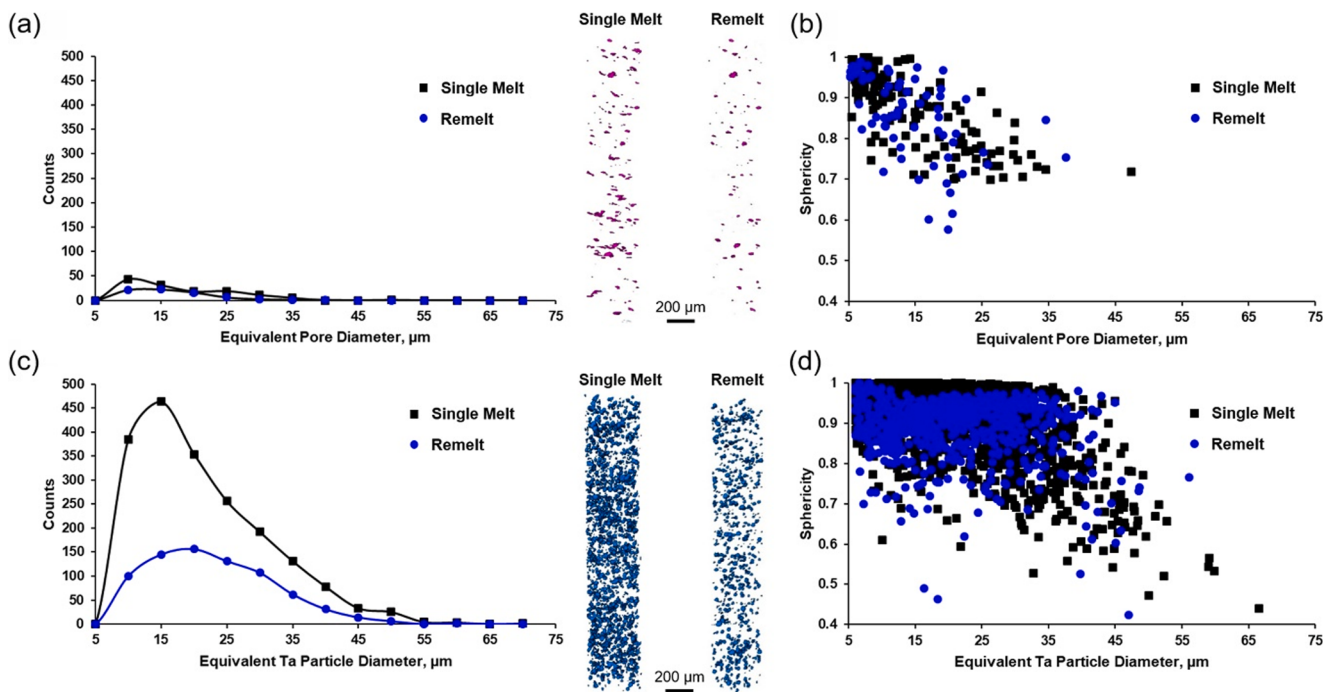


**Fig. 3.** Total counts of porosities (a) and corresponding sphericity (b) for the single melt and remelt Ti65Ta as a function of equivalent diameter analysed by  $\mu$ -CT. The partially melted Ta particle size distribution (c) and the sphericity (d) were analysed as well. The insets show the corresponding reconstructed volume for the single melt and remelt conditions, respectively.

fractured at an elongation of about 10.5 %. In contrast, the remelt scan condition exhibited considerably higher YS and UTS with 940 MPa and 985 MPa, respectively, at the expense of ductility as the specimens failed at 6 %. Both conditions reach their UTS directly after the yield point. Afterwards, necking significantly contributed to the ductility with no considerable strain hardening. Fig. 5 (b) shows the elastic area of the tensile curves, revealing an increased elastic modulus in the remelted condition.

### 3.3. Fatigue behaviour and fractography

To investigate the cyclic mechanical behaviour of the L-PBF Ti65Ta material, low-cycle fatigue testing was conducted at three different strain amplitudes, i.e.,  $\Delta\epsilon_t/2 = \pm 0.5\%$ ,  $\Delta\epsilon_t/2 = \pm 0.65\%$  and  $\Delta\epsilon_t/2 = \pm 0.8\%$  (Fig. 6 (a)). Only one representative curve is shown for the sake of clarity at each strain amplitude for both single melt and remelt conditions. All tests were repeated three times showing very similar stress amplitudes and comparable numbers of cycles to failure. The strain levels were chosen to cover the transition between minor cyclic plastic and merely elastic deformation. Within the first 10 to 20 cycles, the strain amplitude was increased stepwise to avoid buckling of the specimens leading to a steadily increasing stress amplitude in those cycles (not considered in the discussion of results).

A higher total strain amplitude resulted in a reduced fatigue life in both conditions. The single melt Ti65Ta showed a stable stress plateau for all strain amplitudes, whereas a constant stress response was only observed at the lower two total strain amplitudes of  $\Delta\epsilon_t/2 = \pm 0.5\%$  and  $\Delta\epsilon_t/2 = \pm 0.65\%$  for the remelt condition. Softening occurred during cyclic loading for the remelt specimen at the highest strain amplitude ( $\Delta\epsilon_t/2 = \pm 0.8\%$ ). The stress response of the remelt specimens was considerably higher than that of the single melt specimens at an equivalent applied strain amplitude, attributed to the higher strength and the higher elastic modulus of the latter condition (cf. Fig. 5). With a higher strain amplitude the difference in stresses increases, e.g. at  $\Delta\epsilon_t/2 = \pm 0.5\%$  the stress of the remelt specimens is about 50 MPa higher, whereas at  $\Delta\epsilon_t/2 = \pm 0.8\%$  the difference is about 125 MPa. To further

compare the single melt and remelt behaviour, specimens tested at similar stress levels can be compared.

At two distinct stress levels (i.e. 400–450 MPa and 600–625 MPa) the single melt and remelt material showed similar numbers of cycles to failure, eventually indicating very similar fatigue performance, despite the higher strength and reduced ductility of the remelt material. To further assess this aspect, however, additional experiments must be conducted on a statistical basis.

In Fig. 6 (b), the half-life hysteresis curves of the single melt and remelt conditions are displayed for each strain amplitude. The single melt and remelt Ti65Ta showed negligible opening of the hysteresis at all tested strain amplitudes, indicating minimal plastic deformation during cycling. The differing inclination angles of the slope support the results seen in the tensile tests, clearly pointing at a higher elastic modulus in the remelt condition. The elastic modulus was estimated from the hysteresis loops to be  $81.1 \pm 4.9$  GPa and  $96.1 \pm 6.5$  GPa for the single melt and remelt material, respectively.

The fracture surfaces of the LCF specimens were investigated to evaluate whether crack initiation and growth were significantly affected by the pores and/or partially melted particles resolved in the  $\mu$ -CT investigation. The single melt specimen, fatigued with the lowest strain amplitude of 0.5 %, displayed in Fig. 7 (a) exhibited stable crack growth almost across the entire fracture surface. The crack initiated at a defect located at the upper left of the specimen surface (c.f. Fig. 7 (b)). The final failure at the lower right, detailed in Fig. 7 (c), is characterised by dimple-like features. The fracture surface of the remelt specimen at the same strain level is shown in Fig. 7 (d). Crack initiation (Fig. 7 (e)) was also observed at the specimen surface. The area is characterised by a smooth appearance as well, however, the defect in this region is less defined than in the single melt specimen. The area of stable crack growth is considerably smaller than in the single melt Ti65Ta. Rather, the dimples in the area of final failure for the remelt specimen are more distinctive (see Fig. 6 (f)) than in the single melt counterpart.

The single melt specimen loaded at the highest strain amplitude of  $\Delta\epsilon_t/2 = \pm 0.8\%$  (Fig. 7 (g)) revealed a large defect in the area where the crack initiated containing partially melted powder particles (Fig. 7 (h)).

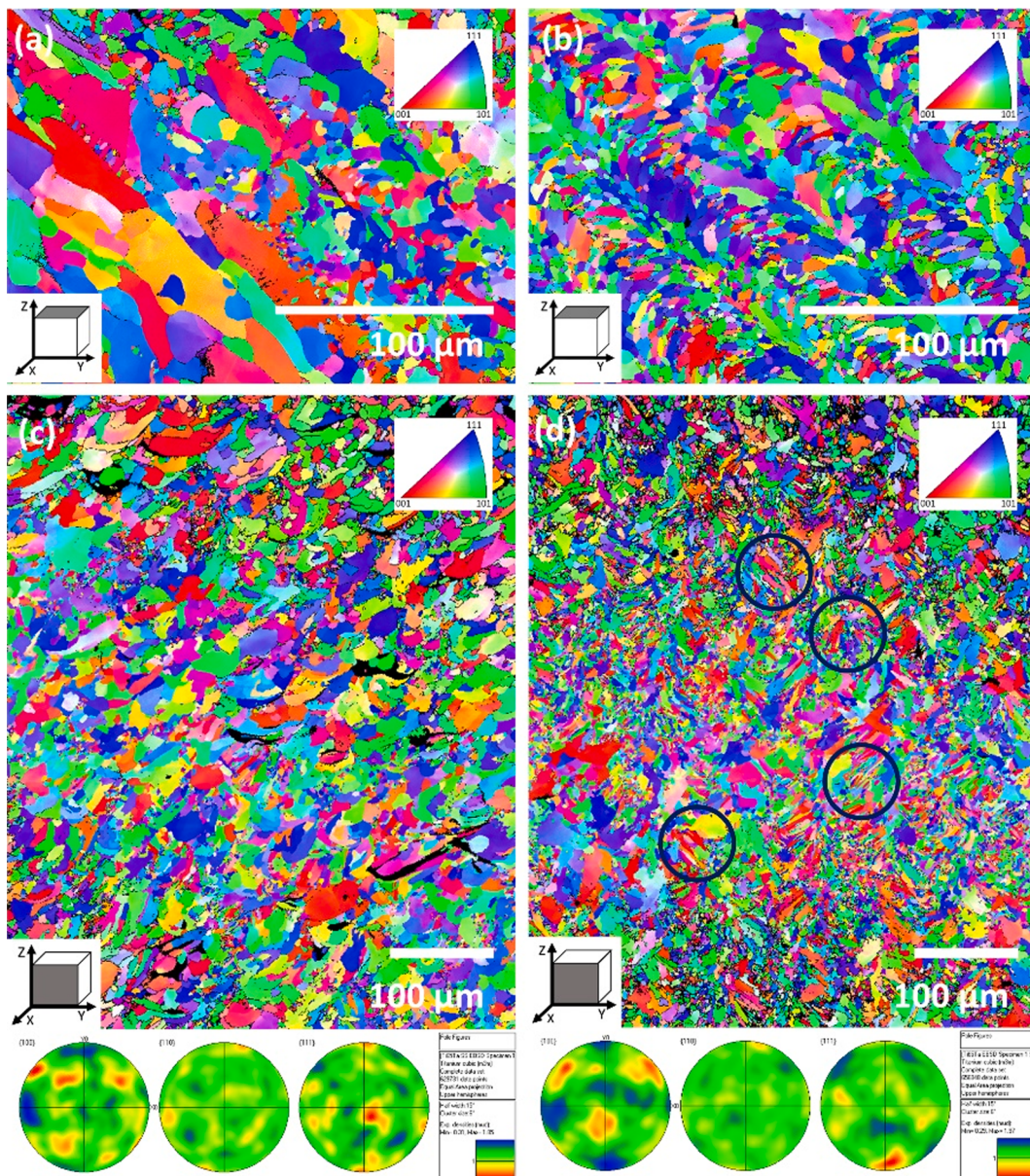


**Fig. 4.** Inverse pole figure maps (IPF) of x-y (a,b) and y-z (c,d) planes of L-PBF Ti65Ta. The single scan microstructure is represented in (a,c) and the remelt scan microstructure is represented in (b,d). Corresponding pole figure plots are shown at the bottom. The black regions notable in (b) correspond to non-indexed areas, as opposed to defects and circled regions indicate radially elongated grains, likely showing direction of heat flow during the second solidification step.

Fatigue striations and shallow dimples are visible in the transition zone in Fig. 7 (i). In the area of final failure minor necking occurred, as deduced from the changed cross-sectional shape of the specimen (Fig. 7 (g)). The fracture surface of the remelt specimen showed at least two crack initialization sites (Fig. 7 (j)) with the most obvious one being detailed in Fig. 7 (k). Within the area of final failure distinct necking occurred and the dimples were most pronounced (c.f. Fig. 7 (l)). In summary, characteristics of all fracture surfaces are indeed very similar, always pointing at process induced porosities being responsible for crack initiation.

#### 4. Discussion

##### 4.1. Optimal processing parameters for Ti65Ta

Processing of mixed powders is a time efficient way of exploring new alloy compositions in L-PBF processing [21]. However, for alloys with refractory components, often not all powder particles are completely

solutionised in matrix material [22–24]. The most common approach to ensure full melting of refractory components is to increase the parameter energy density by increasing the laser power or decreasing the scanning speed. However, this approach is limited by the eventual formation of keyhole porosity when the melt pool penetration becomes too deep and lower melting temperature elements vapourise.

Remelt scanning has been investigated as a promising tool to decrease surface roughness and increase the relative density of refractory alloys. However, a remelting scan also provides an opportunity for partially melted refractory particles to be incorporated into the matrix through a second melting step. When a remelt scan is applied to the Ti65Ta alloy, the effect on material homogeneity can be clearly seen in the reduction in number (~70% reduction) and size of Ta particles (Fig. 3(c) and (d)). The sphericity of the remaining Ta particles also decreases slightly, as partial incorporation of particles in the matrix reduces the number of (initially perfectly shaped plasma atomised) spherical particles left. The positive effect of the remelt scan on increasing homogeneity is similar to that seen in the Ti25Ta alloy, where

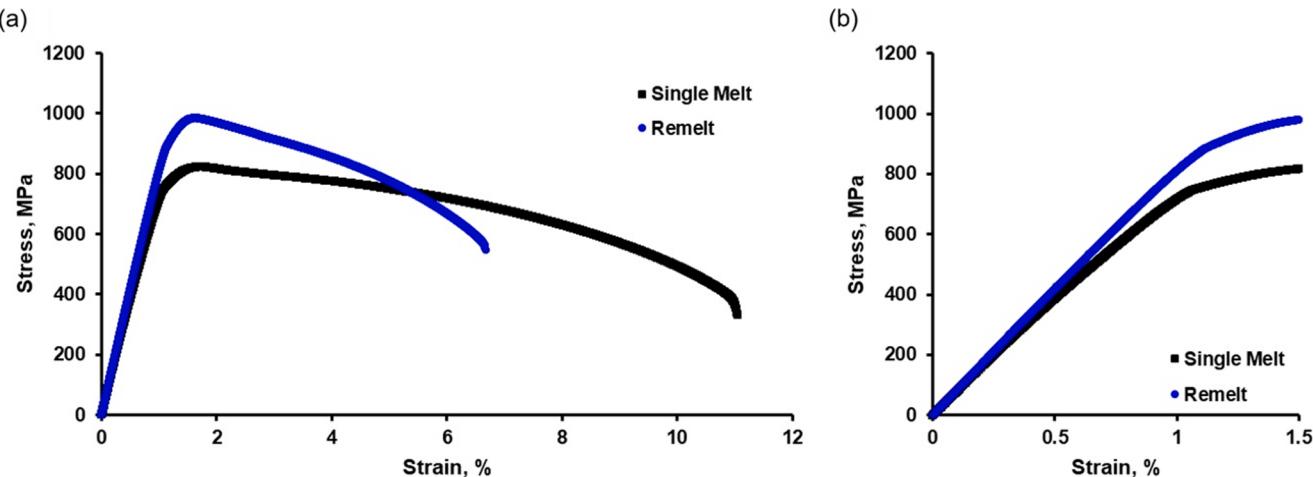


**Fig. 5.** Results from representative tensile tests depicting the behaviour of the small tensile specimens for the single melt and remelt scanning strategies (a); stress–strain behaviour detailing the elastic behaviour (b).

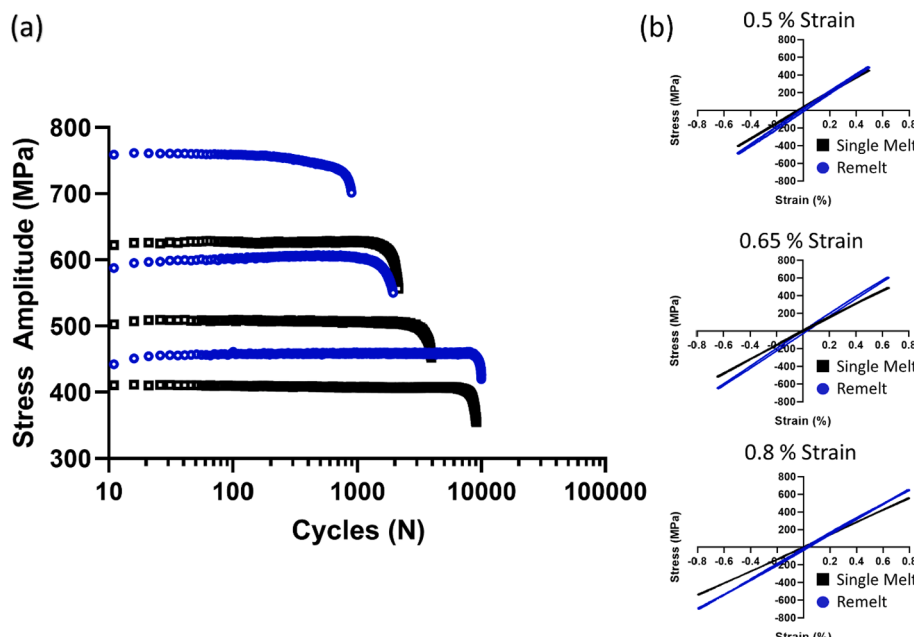


**Fig. 6.** Cyclic deformation response of single and remelt scan Ti65Ta for total strain amplitudes of 0.5%, 0.65% and 0.8% (a) and corresponding half-life hysteresis loops (b).

a ~ 89 % reduction in volume of Ta particles was observed [25].

The effect of the remelt scan on density of the Ti65Ta alloy is negligible. Remelt scanning can cause a significant increase in density of L-PBF refractory materials, such as tungsten, as the second melting step allows for the filling of previous pores, which exist due to insufficient melting during the first scan [26]. Whilst there is a decrease in pores of approximately 10  $\mu\text{m}$  in the Ti65Ta alloy, which could be associated to Ta particles leading to areas of insufficient melting, generally the remelt scan has a negligible effect on the density of this alloy. In comparison, for the Ti25Ta alloy, the remelt scan showed also a minor decrease in density [25].

Despite the almost tripled Ta content of the Ti65Ta powder compared with the Ti25Ta alloy, the optimal processing conditions for each alloy are almost identical. Parameter optimisation was undertaken for the Ti25Ta alloy by adjusting scanning speed by 100 mm/s increments, determining an optimal scanning speed of 300 mm/s for this alloy [20]. Based on the Ti25Ta study, a range of 200 – 400 mm/s was

explored for the Ti65Ta alloy with 50 mm/s increments, and 350 mm/s was determined to be the optimal scanning speed. The normalised enthalpy model proposed by King et al. [27] relates the melting temperature of an alloy to its optimal L-PBF processing parameters, and hence predicts a higher enthalpy and slower scanning speed should be required to process the Ti65Ta alloy. As the increase of Ta content in this mixed powder alloy does not significantly affect the optimal processing conditions, results obtained in the present study indicate that the limitation of processing is linked more closely to laser-powder mechanics, which are not captured in the normalised enthalpy model.

#### 4.2. Microstructure formation in L-PBF Ti65Ta

L-PBF has the tendency to promote columnar grain structures as the heat transfer from melt pool to build plate is strong, leading to epitaxial grain growth and, eventually, evolution of textured material [28]. For smaller specimen sizes, however, the ratio of surface to volume

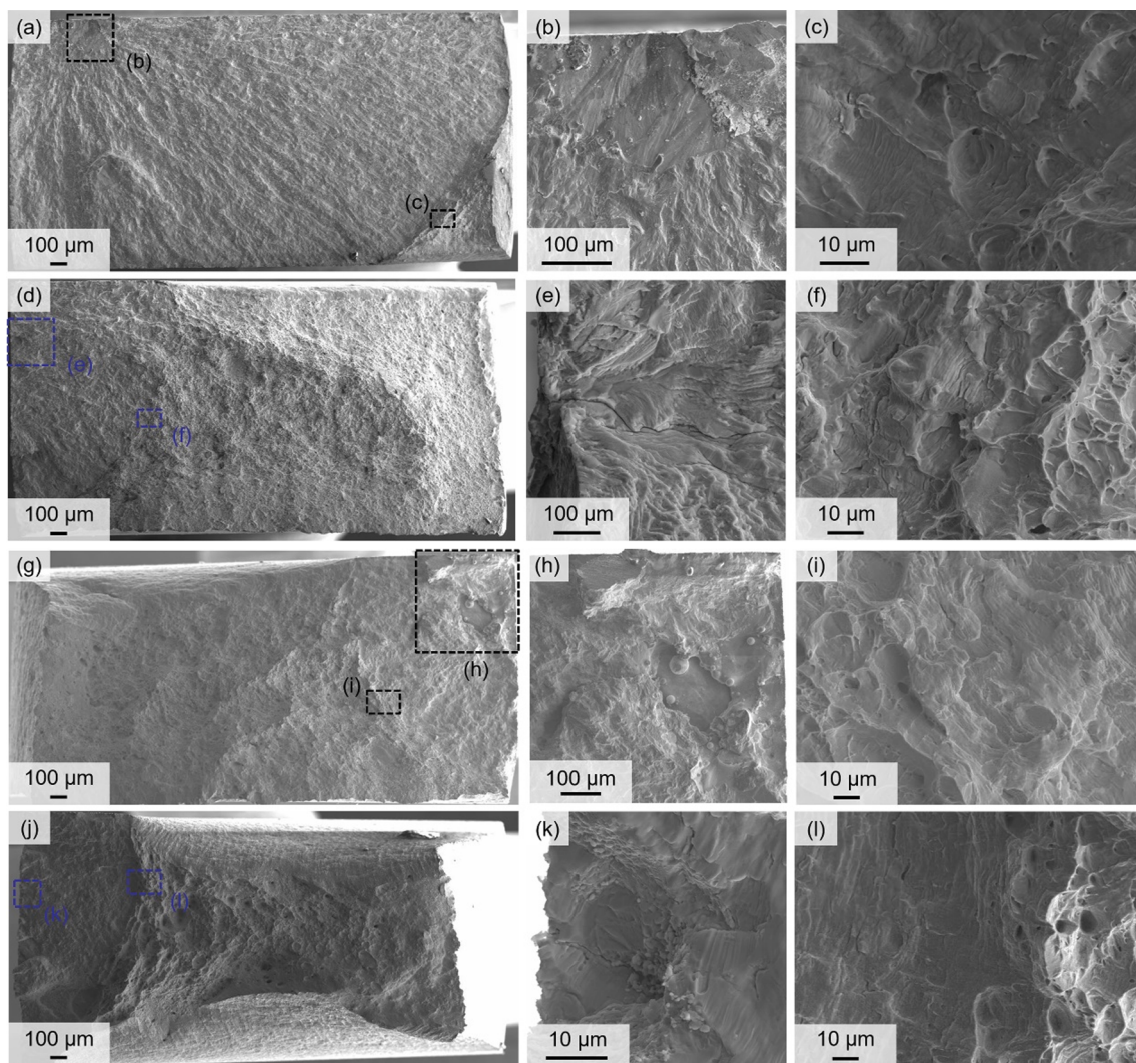


**Fig. 7.** Overview of LCF fracture surfaces of Ti65Ta fatigued with the lowest total strain amplitude ( $\Delta\varepsilon_t/2 = \pm 0.5\%$ ) for the single melt (a) and remelt condition (d). The fracture surfaces for the strain amplitude of  $\Delta\varepsilon_t/2 = \pm 0.8\%$  are displayed for the single melt (g) and remelt (j) conditions. Details showing the corresponding fracture initiation point can be found in (b), (e), (h) and (k). The high-resolution micrographs (c), (f), (i) and (l) highlight characteristic features of the transition area between stable crack growth and final fracture (see boxes in the corresponding overview images).

increases, resulting in a larger portion of randomly oriented contour grains, and hence a lower texture [29]. Despite this benefit, columnar prior- $\beta$  grains are still observed in filigree lattice L-PBF Ti-6Al-4 V structures [29–31], which can lead to anisotropic mechanical properties.

For the Ti65Ta material, columnar grain formation is completely avoided (Fig. 4(c)). The high content of Ta in the Ti65Ta alloy leads to constitutional supercooling dominating thermal transfer as the main driving force for solidification. A similar conclusion was drawn by Sing et al. [22] in a study focusing on L-PBF Ti50Ta, where only equiaxed grains were observed with an average grain size of  $10.20 \pm 7.68\ \mu\text{m}$ . Comparatively, the smaller grain size observed in present work ( $4.8 \pm 5.6\ \mu\text{m}$ ) is likely a combination of the smaller specimen size and the more pronounced compositional driving force for nucleation, due to the higher Ta content. Additionally, remaining partially melted Ta particles act as additional heterogeneous nucleation sites, favouring equiaxed grain formation and a smaller grain size [32].

The remelt scanning strategy caused the grain size to further reduce from  $4.8 \pm 5.6\ \mu\text{m}$  to  $3.3 \pm 2.9\ \mu\text{m}$ . In addition, small regions of thin, elongated grains can be observed which appear to radiate from a central source (circled regions in Fig. 4(d)). It is hypothesised that the remelt scan causes smaller melt pool formation, due to a lower laser energy

absorbed by the reflective solidified metallic surface. Hence, a smaller melt pool may induce faster cooling rates, and hence a stronger driving force for heat-driven solidification at the edge of the melt pool. As a result, grains are formed in the direction of fastest heat transfer, being the closest distance to solidified material through the melt pool wall. A smaller melt pool has also justified the occurrence of grain refinement in remelted Ti-Zr [33], TiC/316L nanocomposites [34], martensitic tool steel [35], Al-Mg-Zr [36] and AlSi10Mg [37,38], however, also resulted in an increased texture in TiAlSn [39]. In the latter study, the increase in texture intensity was attributed to preferential selection of particular  $\alpha'$  variants upon transformation from the  $\beta$  phase, due to a higher stress state caused by the remelt scan. Hence, applying the remelt scan to Ti materials which form an  $\alpha'$  microstructure upon L-PBF processing, (e.g. CP Ti and Ti-6Al-4 V) may enhance anisotropic mechanical behaviour, whilst the Ti65Ta alloy can retain isotropic properties, as evidenced by the corresponding pole figure plots and the low multiples of uniform distribution (MUD) values (cf. Fig. 4), with the additional benefits of refined grain size.

Hence, the remelt scanning strategy is an effective tool in the processing of the Ti65Ta alloy, however, is unlikely to provide much benefit for conventional biomedical alloys such as CP Ti and Ti-6Al-4 V. Comparatively, the strong compositionally driven solidification of the

Ti65Ta alloy allows the formation of a more homogeneous microstructure, which is of high importance for the mechanical behaviour of small metallic implants.

#### 4.3. Mechanical comparison to other L-PBF biomedical alloys

The L-PBF Ti65Ta material showed a considerably higher YS than L-PBF Ti25Ta, commercially pure (CP) Ti and pure Ta (Table 1). Despite this higher YS, the elastic modulus of the alloy was still maintained below 100 GPa, i.e. below that of both CP Ti and pure Ta. The lower modulus can be attributed to the  $\beta$ -crystal structure. The  $\beta$ -crystal structure is less dense compared to the  $\alpha$ -structure of pure Ti (being body-centred cubic (BCC) and hexagonal close packed (HCP), respectively) [40]. Whilst both  $\beta$ -Ti and  $\beta$ -Ta have similar atomic radii (approximately 0.2 nm) and a lattice parameter of approximately 332 ppm [22], the substitution of Ti atoms in the Ta lattice results in a lower elastic modulus for the  $\beta$ -Ti-Ta alloy compared to pure Ta. A low elastic modulus, but high strength, is favoured for small bone facing implants such as mandible plates, as high stresses must be carried by small material volumes, where a lower associated elastic modulus can reduce bone resorption.

Similar to the Ti25Ta alloy, the remelt scan led to an increase in both the strength and elastic modulus of the alloy [25]. The increase in strength is attributed to the reduction in grain size, whilst the increase in elastic modulus is attributed to the increased volume of solutionised Ta. Increasing the Ta content in the  $\beta$ -Ti crystal structure reduces the unit-cell volume, leading to an increase in elastic modulus [45]. However, unlike the Ti25Ta alloy, the Ti65Ta alloy fatigue stress at  $10^6$  cycles increases when the remelt scan is applied. The fatigue behaviour of the remelt Ti25Ta material was believed to decrease primarily due to the decreased alloy ductility, caused by the disruption to martensitic lath organisation [25]. For the  $\beta$ -phase Ti65Ta alloy, a reduction in elongation is also noted when the remelt scan is applied. However, the fatigue performance relative to the YS increases. The difference likely can be attributed to microstructure morphology. The Ti65Ta grain structure is comprised of equiaxed  $\beta$  grains which are significantly refined by the remelt scan, whilst the Ti25Ta material is comprised of  $\alpha'$  laths which do not decrease in width or length when the remelt scan is applied, only a change in misorientation of the laths was observed [20]. As a result, the remelt scan results in an increase in strength of only 119 MPa in the Ti25Ta alloy, compared to 200 MPa for the Ti65Ta alloy. Whilst both alloys decrease in ductility with the remelt scan, the refinement of grains in the Ti65Ta alloy effectively increases the number of obstacles for fatigue crack propagation by increasing the volume of grain boundaries which more effectively slows crack propagation than the misorientation of the  $\alpha'$  laths.

The decrease in size of the remaining partially melted Ta particles, caused by the remelt scan, could also contribute to the increase in fatigue performance of the Ti65Ta remelt alloy. However, the fracture surfaces consistently showed fracture initiation at the specimen surface caused by a defect and not a remaining partially melted Ta particle, similar to the behaviour seen in the Ti25Ta alloy [25]. Hence, it is deduced that the remaining Ta particles have negligible effect on the

fatigue life of the L-PBF TiTa alloys, at least as long as defects prevail in the conditions tested. As the Ta particles show a high level of sphericity and a high capacity for deformation, they do not act as microstructural notches, i.e. stress raising heterogeneities in the matrix.

For biomedical applications, the Ti65Ta alloy remains a good candidate. In situations where thin components are required to carry high stresses, such as thin plates and filigree structures, a high YS is required. Generally, Ti-6Al-4 V is used for these applications, but the remelted Ti65Ta alloy provides the benefit of an improved fatigue life for similar stress levels, likely due to its fine, equiaxed  $\beta$ -grain structure, as well as improved bone integration [14]. Whilst pure Ta and Ti show superior fatigue life performance (normalised to their yield stress), both materials retain a high elastic modulus and low yield strength. For lower strength applications, the L-PBF Ti25Ta material seems to be more suited (in direct comparison to Ti65Ta) due to its low elastic modulus (65% of CP Ti and 35% of Ta) but similar YS and fatigue performance to CP Ti.

#### 4.4. Performance assessment based only on small specimens

In the present study small specimen sizes were used to investigate the mechanical properties of the L-PBF Ti65Ta alloy. Significant cost benefits can arise from using small specimen sizes, especially for difficult to process metals, such as Ta [15]. For conventional manufacturing, the poor workability of Ta increases the cost of complex shaped Ta parts, however, the freedom of design is included in AM processing and hence costs related to workability can be minimised. Although the L-PBF process itself is cost intensive, due to high initial investment, the reduced cost associated with minimised post-processing requirements justifies the use of high cost materials in AM. Furthermore, due to the possibility of reuse of AM powder and hence little material wastage, the high production costs associated with Ta processing are further reduced [46].

However, several influencing factors need to be considered when manufacturing and testing small specimens. As one of the first comprehensive studies, Thompson [47] and Armstrong [48] described a relationship between grain size and specimen size, eventually influencing the resulting mechanical properties. Both defined a critical number of 20 grains within a cross section as the transition between multicrystal to polycrystal material behaviour (for materials without a pronounced texture). Different effects contribute to the sensitivity of mechanical properties to grain size such as, the strengthening character of grain boundaries and the restriction of plastic flow due to neighbouring grains in contrast to free surfaces, i.e. grain constraints. More recently, Molotnikov et al. [49] showed that a ratio of thickness to grain size of at least 20 resulted in mechanical behaviour independent of specimen size.

Furthermore, different materials exhibit different solidification behaviour and hence some are more suitable for studies using small specimen sizes than others. For example, AM face centred cubic (FCC) materials tend to solidify into columnar grains with a pronounced texture, e.g. 316L and Inconel 718, finally promoting a  $\langle 001 \rangle$  texture in the direction of highest cooling rate [50]. For these materials, a

**Table 1**  
Mechanical properties of L-PBF processed biomedical alloys.

|                    | Yield Strength (MPa) | Total Elongation (%) | Elastic Modulus (GPa) | Stress level at $10^6$ cycles* | References |
|--------------------|----------------------|----------------------|-----------------------|--------------------------------|------------|
| Ti65Ta single melt | 740                  | 10.5                 | 81                    | 0.18 $\sigma_y$                | This study |
| Ti65Ta remelt      | 940                  | 6                    | 96                    | 0.23 $\sigma_y$                | This study |
| Ti25Ta single melt | 426                  | 25                   | 65                    | 0.37 $\sigma_y$                | [20,25]    |
| Ti25Ta remelt      | 545                  | 11                   | 77                    | 0.22 $\sigma_y$                | [20,25]    |
| CP Ti              | 555                  | 19.5                 | 104                   | 0.41 $\sigma_y$                | [41–43]    |
| Ta                 | 450–654              | 2                    | 186                   | 0.60 $\sigma_y$                | [41,44]    |
| Ti-6Al-4 V         | 910–1330             | 1.6–11               | 94–118                | 0.12 $\sigma_y$                | [10,41]    |

\* Extrapolated values for stress level at  $10^6$  was obtained from power law curves fitted to the S-N data of the listed L-PBF biomedical alloys (supplementary data Fig. 1).

reduction in specimen size influences the texture of the material due to changes in cooling direction [51,52]. In the case of 316L, the tensile test results of AM small specimens of 3 mm in thickness showed similar properties to ASTM standard wrought specimens, whilst specimens of 1 mm thickness showed reduced values for YS, UTS and elongation at fracture [53]. Furthermore the elongation at fracture was accompanied by pronounced scatter, explained by a reduced number of grains involved in the deformation process leading to an inhomogeneous behaviour and a higher dependency on defect concentration and position [54].

As solidification is compositionally driven in the Ti65Ta L-PBF alloy, effects on mechanical properties caused by elongated grains and texture are avoided [55]. The low grain sizes of the single melt and remelt materials ( $4.8 \pm 5.6 \mu\text{m}$  and  $3.3 \pm 2.9 \mu\text{m}$ , respectively) easily satisfy the conditions for polycrystalline mechanical performance within a 1.5 mm thick specimen and as the specimens were EDM cut from a block, the influence of surface features was significantly reduced. Whilst as-built AM surfaces have been shown to increase the bone bonding capabilities of implant materials [56], it is well known that surface features are detrimental to the mechanical properties of small specimens [29,53,57]. For current applications, small implants are surface finished to a high quality and thus, the AM surface was removed in present work. The optimal balance between surface roughness for bone bonding capabilities and mechanical performance is yet to be determined.

The effect of the remaining partially melted Ta particles on the mechanical properties must also be considered. Defects in small specimens lead to earlier void coalescence during necking and hence reduced tensile elongation [53]. The remelt material showed a slight increase in density but accompanied a decrease in tensile elongation. Thus, it is expected that the defect concentration had negligible effect on the elongation of the Ti65Ta small specimens. The reduced elongation observed is likely due to increased residual stress caused by the remelt scan [39]. Furthermore, as the number of remaining partially melted Ta particles was significantly decreased in the remelt specimen, it is unlikely that these particles are contributing to tensile failure.

For LCF tests, small specimen behaviour has been shown to equate to standard specimen behaviour if a high surface finish is achieved [58]. Hence, the specimens used in present work were EDM machined and polished before testing. The small rectangular cross-section geometry chosen for this study has been previously used for L-PBF fatigue material testing where small material volumes are required [7,59–61]. The rectangular cross-section of the specimen results in fatigue crack initiation at the corners, as the corners experience the highest stress concentration [58]. In the present study however, crack initiation was dominated by defect sites (Fig. 7), commonly seen in the fatigue behaviour of L-PBF materials [59,61–65]. Crack initiation commonly occurs at either surface or internal defect sites. For low ductility materials, such as L-PBF Ti-6Al-4 V, both internal defects and surface defects can lead to sudden failure and hence inferior fatigue life [62,66]. When material ductility is increased, higher stress concentrations experienced by surface defects are required for crack initiation [59,61]. The increased ductility of as-built Ti65Ta as compared to as-built Ti-6Al-4 V results in a lower probability of premature fatigue failure as only severe surface defects act as crack initiation sites and hence the Ti65Ta material likely endures a higher normalised stress level at  $10^6$  cycles than Ti-6Al-4 V ( $0.18 \sigma_y$  to  $0.12 \sigma_y$  respectively). The remelting scan strategy further improves the fatigue behaviour of the Ti65Ta alloy by reducing the number of surface defect crack initiation sites.

## 5. Conclusion

A mixed powder Ti65Ta alloy was produced by L-PBF and its microstructure investigated by optical microscopy, SEM and  $\mu$ -CT analysis. Small specimens for mechanical testing were machined from manufactured blocks processed with two different scanning strategies (single melt and remelt). Tensile and low-cycle fatigue behaviour were

investigated to assess the suitability of the L-PBF alloy for small biomedical implants. The results can be summarized as follows:

- Ti65Ta material was produced with density  $> 99.88\%$ . The remelt scan strategy improved material homogeneity without any concomitant loss in density.
- A fully  $\beta$  phase, non-columnar microstructure was observed with a grain size of  $4.8 \pm 5.6 \mu\text{m}$  and weak texture. The remelt scan refined the grain size to  $3.3 \pm 2.9 \mu\text{m}$  and had negligible effect on texture.
- The L-PBF material showed a higher tensile strength than both L-PBF Ti and Ta and the remelt scan increased the yield strength to a value similar to that of L-PBF Ti-6Al-4 V through grain refinement.
- The single melt and remelt material showed a similar number of cycles to failure under similar stress levels.
- The small specimen geometry was deemed adequate to represent the fatigue properties of L-PBF Ti65Ta small biomedical implants although further studies on the trade-off between surface roughness and bone integration are required for optimisation of AM implants.

## Declaration of Competing Interest

The authors declare that they have no known competing financial interests or personal relationships that could have appeared to influence the work reported in this paper.

## Acknowledgements

EGB would like to acknowledge the use of instruments and scientific and technical assistance at the Monash Centre for Electron Microscopy, a Node of Microscopy Australia. This project is funded by the ARC Research Hub for Transforming Australia's Manufacturing Industry through High Value Additive Manufacturing (IH130100008). AM would also like to acknowledge the support of the Garnett Passe and Rodney Williams Memorial Foundation 2019 Conjoint Grant. TN acknowledges financial support by AiF/IGF (Contract # 19689 BG/2).

## Appendix A. Supplementary material

Supplementary data to this article can be found online at <https://doi.org/10.1016/j.ijfatigue.2022.106944>.

## References

- [1] DebRoy T, Wei HL, Zuback JS, Mukherjee T, Elmer JW, Milewski JO, et al. Additive manufacturing of metallic components – Process, structure and properties. *Prog Mater Sci* 2018;92:112–224.
- [2] Yap CY, Chua CK, Dong ZL, Liu ZH, Zhang DQ, Loh LE, et al. Review of selective laser melting: Materials and applications. *Appl Phys Rev* 2015;2(4):041101.
- [3] Hitzler L, Merkel M, Hall W, Öchsner A. A Review of Metal Fabricated with Laser- and Powder-Bed Based Additive Manufacturing Techniques: Process, Nomenclature, Materials, Achievable Properties, and its Utilization in the Medical Sector. *Adv Eng Mater* 2018;20(5):1700658.
- [4] Bartlett JL, Li X. An overview of residual stresses in metal powder bed fusion. *Addit Manuf* 2019;27:131–49.
- [5] Brenne F, Niendorf T. Damage tolerant design by microstructural gradation – Influence of processing parameters and build orientation on crack growth within additively processed 316L. *Mater Sci Eng, A* 2019;764:138186.
- [6] Soro N, Saintier N, Merzeau J, Veidt M, Dargusch MS. Quasi-static and fatigue properties of graded Ti-6Al-4V lattices produced by Laser Powder Bed Fusion (LPBF). *Addit Manuf* 2021;37:101653.
- [7] Richter J, Sajadifar SV, Niendorf T. On the influence of process interruptions during additive manufacturing on the fatigue resistance of AlSi12. *Addit Manuf* 2021;47:102346.
- [8] Melancon D, Bagheri ZS, Johnston RB, Liu L, Tanzer M, Pasini D, Mechanical characterization of structurally porous biomaterials built via additive manufacturing: experiments, predictive models, and design maps for load-bearing bone replacement implants. *Acta Biomater*. 63(Supplement C) (2017) 350–368.
- [9] Lowther M, Louth S, Davey A, Hussain A, Ginestra P, Carter L, et al. Clinical, industrial, and research perspectives on powder bed fusion additively manufactured metal implants. *Addit Manuf* 2019;28:565–84.
- [10] Beese AM, Carroll BE. Review of Mechanical Properties of Ti-6Al-4V Made by Laser-Based Additive Manufacturing Using Powder Feedstock. *JOM* 2016;68(3):724–34.

- [11] Polmear IJ, StJohn D, Nie J, Qian M. Titanium Alloys, Light Alloys: Metallurgy of the Light Metals. Oxford: Butterworth-Heinemann; 2017. p. 369–459.
- [12] Tang Z, Xie Y, Yang F, Huang Y, Wang C, Dai K, et al. Porous Tantalum Coatings Prepared by Vacuum Plasma Spraying Enhance BMSCs Osteogenic Differentiation and Bone Regeneration In Vitro and In Vivo. *PLoS ONE* 2013;8(6):e66263.
- [13] Tae-Sik J, Hyun-Do J, Sungwon K, Byeong-Seok M, Jaek B, Cheonil P, et al. Multiscale porous titanium surfaces via a two-step etching process for improved mechanical and biological performance. *Biomed Mater* 2017;12(2):025008.
- [14] Brodie EG, Robinson KJ, Sigston E, Molotnikov A, Frith JE. Osteogenic Potential of Additively Manufactured TiTa Alloys. *ACS Appl Bio Mater* 2021;4(1):1003–14.
- [15] Davis JM, Saei M, Mohanty DP, Udupa A, Sugihara T, Chandrasekar S. Cutting of tantalum: Why it is so difficult and what can be done about it. *Int J Mach Tools Manuf* 2020;157:103607.
- [16] Mascha F, Winter K, Pietzka S, Heufelder M, Schramm A, Wilde F. Accuracy of computer-assisted mandibular reconstructions using patient-specific implants in combination with CAD/CAM fabricated transfer keys. *J Craniomaxillofac Surg* 2017;45(11):1884–97.
- [17] Thijs L, Montero Sistiaga ML, Wauthle R, Xie Q, Kruth J-P, Van Humbeeck J. Strong morphological and crystallographic texture and resulting yield strength anisotropy in selective laser melted tantalum. *Acta Mater* 2013;61(12):4657–68.
- [18] Seifi M, Goretlik M, Waller J, Hrabe N, Shamsaei N, Daniewicz S, et al. Progress towards metal additive manufacturing standardization to support qualification and certification. *JOM* 2017;69(3):439–55.
- [19] Niendorf T, Brenne F, Schaper M. Lattice Structures Manufactured by SLM: On the Effect of Geometrical Dimensions on Microstructure Evolution During Processing. *Metall Mater Trans B* 2014;45(4):1181–5.
- [20] Brodie EG, Medvedev AE, Frith JE, Dargusch MS, Fraser HL, Molotnikov A. Remelt processing and microstructure of selective laser melted Ti25Ta. *J Alloys Compd* 2020;820:153082.
- [21] Zhang T, Huang Z, Yang T, Kong H, Luan J, Wang A, et al. In situ design of advanced titanium alloy with concentration modulations by additive manufacturing. *Science* 2021;374(6566):478–82.
- [22] Sing SL, Yeong WY, Wiria FE. Selective laser melting of titanium alloy with 50 wt% tantalum: Microstructure and mechanical properties. *J Alloys Compd* 2016;660: 461–70.
- [23] Liu YJ, Li XP, Zhang LC, Sercombe TB. Processing and properties of topologically optimised biomedical Ti-24Nb-4Zr-8Sn scaffolds manufactured by selective laser melting. *Mater Sci Eng A* 2015;642:268–78.
- [24] Duan R, Li S, Cai B, Zhu W, Ren F, Attallah MM. A high strength and low modulus metastable  $\beta$  Ti-12Mo-6Zr-2Fe alloy fabricated by laser powder bed fusion in-situ alloying. *Addit Manuf* 2021;37:101708.
- [25] Brodie EG, Richter J, Wegener T, Niendorf T, Molotnikov A. Low-cycle fatigue performance of remelted laser powder bed fusion (L-PBF) biomedical Ti25Ta. *Mater Sci Eng A* 2020;798:140228.
- [26] Xiong Z, Zhang P, Tan C, Dong D, Ma W, Yu K. Selective Laser Melting and Remelting of Pure Tungsten. *Adv Eng Mater* 2020;22(3):1901352.
- [27] King WE, Barth HD, Castillo VM, Gallegos GF, Gibbs JW, Hahn DE, et al. Observation of keyhole-mode laser melting in laser powder-bed fusion additive manufacturing. *J Mater Process Technol* 2014;214(12):2915–25.
- [28] Bermingham MJ, StJohn DH, Krynen J, Tedman-Jones S, Dargusch MS. Promoting the columnar to equiaxed transition and grain refinement of titanium alloys during additive manufacturing. *Acta Mater* 2019.
- [29] Barba D, Alabot C, Tang YT, Viscasillas MJ, Reed RC, Alabot E. On the size and orientation effect in additive manufactured Ti-6Al-4V. *Mater Des* 2020;186: 108235.
- [30] Kelly CN, Kahra C, Maier HJ, Gall K. Processing, structure, and properties of additively manufactured titanium scaffolds with gyroid-sheet architecture. *Addit Manuf* 2021;41:101916.
- [31] Jin N, Yan Z, Wang Y, Cheng H, Zhang H. Effects of heat treatment on microstructure and mechanical properties of selective laser melted Ti-6Al-4V lattice materials. *Int J Mech Sci* 2021;190:106042.
- [32] Tedman-Jones SN, McDonald SD, Bermingham MJ, StJohn DH, Dargusch MS. A new approach to nuclei identification and grain refinement in titanium alloys. *J Alloys Compd* 2019;794:268–84.
- [33] Yao Y, Li X, Wang YY, Zhao W, Li G, Liu RP. Microstructural evolution and mechanical properties of Ti-Zr beta titanium alloy after laser surface remelting. *J Alloys Compd* 2014;583:43–7.
- [34] AlMangour B, Grzesiak D, Yang J-M. Scanning strategies for texture and anisotropy tailoring during selective laser melting of TiC/316L stainless steel nanocomposites. *J Alloys Compd* 2017;728:424–35.
- [35] Chen H, Gu D, Dai D, Xia M, Ma C. A novel approach to direct preparation of complete lath martensite microstructure in tool steel by selective laser melting. *Mater Lett* 2018;227:128–31.
- [36] Griffiths S, Rossell MD, Croteau J, Vo NQ, Dunand DC, Leinenbach C. Effect of laser rescanning on the grain microstructure of a selective laser melted Al-Mg-Zr alloy. *Mater Charact* 2018;143:34–42.
- [37] Liu B, Li B-Q, Li Z. Selective laser remelting of an additive layer manufacturing process on AlSi10Mg. *Results Phys* 2019;12:982–8.
- [38] Guan J, Jiang Y, Zhang X, Chong X. Microstructural evolution and EBSD analysis of AlSi10Mg alloy fabricated by selective laser remelting. *Mater Charact* 2020;161: 110079.
- [39] Wei K, Lv M, Zeng X, Xiao Z, Huang G, Liu M, et al. Effect of laser remelting on deposition quality, residual stress, microstructure, and mechanical property of selective laser melting processed Ti-5Al-2.5Sn alloy. *Mater Charact* 2019;150: 67–77.
- [40] Niinomi M, Nakai M, Hieda J. Development of new metallic alloys for biomedical applications. *Acta Biomater* 2012;8(11):3888–903.
- [41] Wauthle R, Ahmadi SM, Amin Yavari S, Mulier M, Zadpoor AA, Weinans H, et al. Revival of pure titanium for dynamically loaded porous implants using additive manufacturing. *Mater Sci Eng* 2015;C 54(C):94–100.
- [42] Attar H, Calin M, Zhang LC, Scudino S, Eckert J, Manufacture by selective laser melting and mechanical behavior of commercially pure titanium, *Mater. Sci. Eng. A* 593(Supplement C) (2014) 170–177.
- [43] Attar H, Bermingham MJ, Ehtemam-Haghghi S, Dehghan-Manshadi A, Kent D, Dargusch MS. Evaluation of the mechanical and wear properties of titanium produced by three different additive manufacturing methods for biomedical application. *Mater Sci Eng A* 2019;760:339–45.
- [44] Zhou L, Yuan T, Li R, Tang J, Wang G, Guo K, Selective laser melting of pure tantalum: Densification, microstructure and mechanical behaviors, *Mater. Sci. Eng. A* 707(Supplement C) (2017) 443–451.
- [45] Zhou YL, Niinomi M, Akahori T. Effects of Ta content on Young's modulus and tensile properties of binary Ti-Ta alloys for biomedical applications. *Mater Sci Eng A* 2004;371(1–2):283–90.
- [46] Bergonzi L, Vettori M, Pirondi A. Development of a miniaturized specimen to perform uniaxial tensile tests on high performance materials. *Procedia Struct Integr* 2019;24:213–24.
- [47] Thompson AW. Use of non-polycrystal specimens in mechanical behavior tests. *Scr Metall* 1974;8(2):145–7.
- [48] Armstrong RW. On size effects in polycrystal plasticity. *J Mech Phys Solids* 1961;9 (3):196–9.
- [49] Molotnikov A, Lapovok R, Davies CHJ, Cao W, Estrin Y. Size effect on the tensile strength of fine-grained copper. *Scripta Mater* 2008;59(11):1182–5.
- [50] Hu H. Texture of Metals. *Texture* 1974;1:753983.
- [51] Brenne F, Niendorf T. Effect of notches on the deformation behavior and damage evolution of additively manufactured 316L specimens under uniaxial quasi-static and cyclic loading. *Int J Fatigue* 2019;127:175–89.
- [52] Leicht A, Klement U, Hryha E. Effect of build geometry on the microstructural development of 316L parts produced by additive manufacturing. *Mater Charact* 2018;143:137–43.
- [53] Leicht A, Pauzon C, Rashidi M, Klement U, Nyborg L, Hryha E. Effect of part thickness on the microstructure and tensile properties of 316L parts produced by laser powder bed fusion. *Adv Ind Manuf Eng* 2021;2:100037.
- [54] Chan WL, Fu MW. Experimental studies and numerical modeling of the specimen and grain size effects on the flow stress of sheet metal in microforming. *Mater Sci Eng A* 2011;528(25):7674–83.
- [55] Brodie EG, Wegener T, Richter J, Medvedev A, Niendorf T, Molotnikov A. A mechanical comparison of alpha and beta phase biomedical TiTa lattice structures. *Mater Des* 2021;212:110220.
- [56] Zhang L-C, Attar H. Selective Laser Melting of Titanium Alloys and Titanium Matrix Composites for Biomedical Applications: A Review *Adv. Eng Mater* 2016;18 (4):463–75.
- [57] Becker TH, Kumar P, Ramamurty U. Fracture and Fatigue in Additively Manufactured Metals. *Acta Mater* 2021;117240.
- [58] Nozaki M, Sakane M, Fujiwara M. Low cycle fatigue testing using miniature specimens. *Int J Fatigue* 2020;137:105636.
- [59] Wegener T, Koopmann J, Richter J, Kroob P, Niendorf T. CuCrZr processed by laser powder bed fusion—Processability and influence of heat treatment on electrical conductivity, microstructure and mechanical properties. *Fatigue Fract Eng Mater Struct* 2021;44(9):2570–90.
- [60] Picak S, Wegener T, Sajadifar SV, Sobrero C, Richter J, Kim H, et al. On the low-cycle fatigue response of CoCrNiFeMn high entropy alloy with ultra-fine grain structure. *Acta Mater* 2021;205:116540.
- [61] Wegener T, Brenne F, Fischer A, Möller T, Hauck C, Auernhammer S, et al. On the structural integrity of Fe-36Ni Invar alloy processed by selective laser melting. *Addit Manuf* 2021;37:101603.
- [62] Günther J, Krewerth D, Lippmann T, Leuders S, Tröster T, Weidner A, Biermann H, Niendorf T, Fatigue life of additively manufactured Ti-6Al-4V in the very high cycle fatigue regime, *Int. J. Fatigue* 94(Part 2) (2017) 236–245.
- [63] Benedetti M, Fontanari V, Bandini M, Zanini F, Carmignato S. Low- and high-cycle fatigue resistance of Ti-6Al-4V ELI additively manufactured via selective laser melting: Mean stress and defect sensitivity. *Int J Fatigue* 2018;107:96–109.
- [64] Beretta S, Romano S. A comparison of fatigue strength sensitivity to defects for materials manufactured by AM or traditional processes. *Int J Fatigue* 2017;94: 178–91.
- [65] Greitemeier D, Palm F, Syassen F, Melz T. Fatigue performance of additive manufactured TiAl6V4 using electron and laser beam melting. *Int J Fatigue* 2017; 94:211–7.
- [66] Leuders S, Thöne M, Riemer A, Niendorf T, Tröster T, Richard HA, et al. On the mechanical behaviour of titanium alloy TiAl6V4 manufactured by selective laser melting: Fatigue resistance and crack growth performance. *Int J Fatigue* 48 (Supplement C) (2013) 300–7.